A transient analysis of a micro-tubular solid oxide fuel cell (SOFC)

Mustafa Fazil Serincan [a,*], Ugur Pasaogullari [a], Nigel M. Sammes [b]

[a] Department of Mechanical Engineering, and Connecticut Global Fuel Cell Center, University of Connecticut, 44 Weaver Rd Unit 5233, Storrs, CT 06269, USA
[b] Department of Metallurgical and Materials Engineering, Colorado School of Mines, 1500 Illinois St, Golden, CO 80401, USA

ARTICLE INFO

ABSTRACT

A two-dimensional, axisymmetric transient computational fluid dynamics model is developed for an intermediate temperature micro-tubular solid oxide fuel cell (SOFC), which incorporates mass, species, momentum, energy, ionic and electronic charge conservation. In our model we also take into account internal current leak which is a common problem with ceria based electrolytes. The current density response of the SOFC as a result of step changes in voltage is investigated. Time scales associated with mass transfer and heat transfer are distinguished in our analysis while discussing the effect of each phenomenon on the overall dynamic response. It is found that the dynamic response is controlled by the heat transfer. Dynamic behavior of the SOFC as a result of failure in fuel supply is also investigated, and it is found that the external current drops to zero in less than 1 s.

1. Introduction

Solid oxide fuel cells are among the prominent candidates for an alternative power generation method due to fuel flexibilities [1,2] and their capabilities to be used in cogeneration applications for increased system efficiencies [3–5]. On the other hand SOFCs with micro-tubular design are accepted as more favorable than planar SOFCs because of their better sealing capabilities and enhanced thermo-cycling characteristics [6]. Improvement in thermal management and reduction of the losses [7,8] due to their sub-millimeter dimensions are also reported as a superiority over the planar design.

Although significant amount of work exist on micro-tubular SOFCs [9–16], these devices are not employed in any practical applications yet due to lack of operation optimization to maintain electrochemical performance and mechanical durability simultaneously. This is also related to the difficulty in experimentation as the data such as temperature and current distribution, is not so easily measurable due to the smaller dimensions and elevated operating temperatures. Consequently, modeling becomes the primary tool to develop essential insight into operation since one can acquire information at a specific point inside the cell through modeling. For example, it is valuable to predict where the maximum temperature occurs during the fuel cell operation from a thermal stress perspective. Furthermore, employing modeling to understand the

dynamic behavior of the cell is necessary because it is vital to maintain mechanical stability of the cell during any proposed operation hence it is essential to track the changes in temperature with time at any location inside the cell. Helping to understand the transient physical phenomena inside the fuel cell, modeling becomes an important tool to predict the response of fuel cell parameters to any load change and then can be used to suggest a control scheme for the fuel cell operation. Modeling can also be utilized to identify the fuel cell behavior at some critical conditions such as failures in system components.

While there are a number of significant modeling efforts, both in steady state [17–24] and in transient [25–33], transient SOFC models typically are not as elaborate as steady-state models. Some of the transient models are lumped models [34,35] neglecting all the spatial variations. They are mainly developed for control or to simulate the fuel cell as part of the larger system. Transient models incorporating transport phenomena vary from one-dimensional to three-dimensional models. 3D models are developed generally for planar SOFC, whereas exploiting the axial symmetry of the tubes, two-dimensional models are preferred and most of the time sufficient to represent a SOFC with a tubular design.

Achenbach presented one of the first transient studies on SOFCs [26]. He developed a 3D transient model to investigate the voltage responses of a planar SOFC to certain load changes. Ioara et al. developed a 1-D model for a planar direct internal reforming SOFC in which they concluded that neglecting the variation of the gas stream properties may lead to incorrect dynamic response predictions [27].

* Corresponding author. Tel.: +1 86 09493526; fax: +1 86 04868378.
E-mail address: fazil.serincan@uconn.edu (M.F. Serincan).

Nomenclature

Symbols

k	thermal conductivity
T	temperature
C_p	specific heat
u	velocity vector
Q	volumetric heat source
p	pressure
l	unit vector
g	gravity
R	volumetric consumption
w	species mass fraction
x	species mole fraction
n	number of species
F	Faraday constant
R	universal gas constant
i	exchange current density
A	pre-exponential constant
EA	Electrode activation energy
k_b	Boltzmann constant
h	enthalpy
M	molecular weight
r_p	average pore radius

Greek

ρ	density
μ	dynamic viscosity
κ	permeability
σ	conductivity
φ	potential
γ	concentration dependency
α	transfer coefficient
η	overpotential
ε	porosity
τ	tortuosity

Subscripts

a	anode
c	cathode
elc	electrolyte
j	species
k	species
i	ionic
e	electronic
eq	equilibrium
eff	effective
Kn	Knudsen

Superscripts

for	formation
in	inlet
reac	reacted
T	transpose
Th	thermal

Jia et al. provides detailed analysis of the effects of operating parameters on the steady state and transient performance of a tubular SOFC [29]. Employing a 1D model they represented the conservation laws with a control volume approach. In a recent study of Barzi et al. [28] dynamic responses of a tubular SOFC are predicted during the startup. Their 2D model incorporates mass, momentum and species balances accompanied with a circuit representation of charge balances. Bhattacharyya et al. compared the dynamic behav-ior of the cell with the experiments in their 2D model of a tubular SOFC [30]. Along with investigating dynamic response of the cell to the changes in voltage, they also predicted the response of the cell to the changes in hydrogen flow rate.

Ota et al. compared transient characteristics of a standard tubular cell with a micro-tubular cell with a modeling framework presented therein [31]. Their modeling framework is based on simplifications instead of taking into account full coupling of the sophisticated transport phenomena. They reported that time scales of a standard tubular cell to a specific voltage response is six times larger than that of a micro-tubular cell. Another modeling study on micro-tubular SOFCs is presented by Nehter [32]. In this study, he compared a common micro-tubular cell with a cascaded one. Although localized temperature and species concentrations are provided in his 2D axial symmetric model, momentum balance and multicomponent species transfer are not included. Mass balance is carried out in a simple way via algebraic equations describing the electrochemical and shift reactions.

Although there are many simplifications in the models of Ota et al. and Nehter, their studies are significant since, to the knowledge of the authors, they are the only modeling efforts emphasized dynamics of micro-tubular SOFCs. Since the characteristics of a micro-tubular SOFC are very different than a standard tubular cell, there is still need for a rigorous model to study the dynamics of a micro-tubular cell. Therefore in our study, we extend our previous modeling framework [36,37] to a transient model to study the dynamic behavior of a micro-tubular SOFC. The model incorporates mass, species, momentum and energy balances along with electrochemical kinetics and ionic and electronic charge conservations. Taking into account full coupling between these physical phenomena, model equations are solved in a distributed space and time domain. Due to the axial symmetry of the tubular geometry, the model is constructed in a two-dimensional axisymmetric domain by assuming the anode and the cathode current collectors are uniformly distributed on the electrode surfaces. Simulations are then carried out to analyze the dynamic response of the micro-tubular fuel cell and predict the evolution of the temperature and hydrogen concentration profiles as a result of voltage changes. In addition, we investigate a failure scenario in which the flow in the fuel channel is cut off suddenly due to a probable malfunction in the fuel supply system.

2. Mathematical model

As shown in Fig. 1, model geometry includes the anode tube and the fuel channel, the electrolyte, the cathode and the air chamber and the supporting alumina tubes. Fig. 1 (not drawn to scale) shows the cross-section of the axial symmetric geometry. The actual model geometry can be visualized by revolving this cross-section around the symmetry axis, i.e. centerline of the anode tube. Mass, species and momentum conservation equations are solved in the gas channels and the porous electrodes, and energy conservation is applied in the entire domain. Ionic charge balance is applied in the anode, the electrolyte and the cathode whereas the electronic charge balance is applied in the anode and cathode.

In this study, we model the micro-tubular cells which are fabricated and characterized by the New Energy Development Organization (NEDO) of Japan under the Advanced Ceramic Reactor Program. The anode supported cells employs a $Ce_{0.9}Gd_{0.1}O_{1.95-\delta}$ (GDC) electrolyte coated on a NiO-GDC anode, and $La_{0.8}Sr_{0.2}Co_{0.6}Fe_{0.4}O_3$ (LSCF)-GDC cathode. It is well-known that GDC electrolytes are prone to internal current leaks. GDC becomes reduced and electronically conductive under certain conditions, especially at elevated temperatures [38]. Fraction of the electrons generated at the anode is then transferred to the cathode through
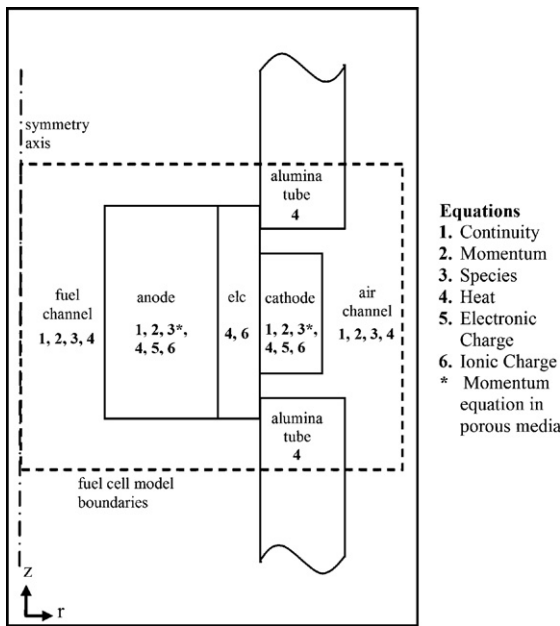
Fig. 1. Model geometry and the equations solved in the model. Model geometry is the same as the one in our previous study and above figure is the same as Fig. 1b of Ref. [36].

the electrolyte. As a result the cell is short circuited and drop in open circuit voltage is experienced. The effect of current leaks becomes less significant at higher current densities, because they are inversely proportional to the ionic current density [39]. Here, we model the electronic current leaks as boundary conditions to the electronic charge equation at the electrolyte interfaces of anode and cathode, which will be explained later while describing the boundary conditions.

The mathematical model is summarized below. However, for the details of the equations and the modeling framework that includes a realistic model of the actual fuel cell test environment, we refer to our previous studies [36,37].

2.1. Mass and momentum conservation

Continuity equation is solved coupled with non-isothermal momentum equation to account for mass and momentum balances respectively.

$$\frac{d(\varepsilon\rho)}{dt} + \nabla \cdot (\rho\mathbf{u}) = \sum_j R_j \tag{1}$$

$$\frac{d}{dt}\left(\frac{\rho\mathbf{u}}{\varepsilon}\right) + \rho\mathbf{u} \cdot \nabla\mathbf{u} = \nabla \cdot \left[-p\mathbf{I} + \frac{\mu}{\varepsilon}(\nabla\mathbf{u} + (\nabla\mathbf{u})^T) - \frac{2\mu}{3}(\nabla \cdot \mathbf{u})\mathbf{I}\right] + \rho\mathbf{g} - \left(\frac{\mu}{K}\right)\mathbf{u} + \mathbf{F} \tag{2}$$

In Eq. (2), right hand side describes the surface (pressure and shear) forces, body forces, Darcy's term accounting for the additional pressure drop in porous media and any other forces acting on the fluid, **F**. The above equations are written in a general form which can be applied to both gas channels and porous electrodes. In gas channels, porosity, ε is taken to be unity while, permeability, K is infinity. Source terms appearing in Eqs. (1) and (2) as well as the ones for the other conservation equations are given in Table 1.

Density is calculated for a multicomponent mixture by:

$$\rho = \frac{p}{RT}\sum_j x_j M_j \tag{3}$$

where x_j is the mole fraction of the species determined from the species balance and M_j is the molecular weight of the species.

2.2. Species conservation

In this work, Maxwell-Stefan equations are utilized for species conservation:

$$\frac{d(\varepsilon\rho w_j)}{dt} + \nabla \cdot \left[\rho w_j\mathbf{u} - \rho w_j\sum_{k=1}^{n}\tilde{D}_{jk}\left(\nabla x_k + (x_k - w_k)\frac{\nabla p}{p}\right)\right] = R_j \tag{4}$$

Eq. (4) represents a set of partial differential equations solved for $n-1$ species in a multicomponent gas mixture of n species. The mass fraction of the nth species is calculated via:

$$\sum_{j=1}^{n} w_j = 1 \tag{5}$$

In the fuel channel Eq. (4) is solved for hydrogen and water, whereas in the air chamber it is solved for oxygen and water. Nitrogen is the background (nth) species for both mixtures. In the form of Maxwell-Stefan equations developed by Curtiss and Bird [40], second term inside the brackets on the right hand side is defined as the diffusion driving force. Derivation of the above term, valid for ideal gases can be found in Ref. [40]. $\tilde{D}_{jk}$ in Eq. (4) are the Maxwell-Stefan diffusivities and calculated from binary diffusion coefficients for each species pair. Binary diffusion coefficients are calculated using Fuller's method [41,42] which is reported to match the experimental data better at high temperatures [43].

$$D_{jk} = \frac{0.00143T^{1.75}}{pM_{jk}^{1/2}(V_j^{1/3} + V_k^{1/3})^2} \tag{6}$$

in which p is the gas pressure and T is the temperature, in bars and K, respectively. D_{jk} is calculated in $m^2\,s^{-1}$ from this expression. M_{jk} is defined as the combined molecular weight of the gas pair and can be calculated as $M_{jk} = 2[1/M_j + 1/M_k]^{-1}$. V_j are the special diffusion volumes of Fuller et al. [41], which are listed for SOFC gases in Ref. [44]. Binary diffusivities are then corrected to account for mass transfer resistance in porous media via the following relation:

$$D_{jk}^{eff} = \frac{\varepsilon}{\tau}D_{jk} \tag{7}$$

where ε is the porosity and τ is the tortuosity and listed in Table 2. Porosity values for unreduced anode and cathode are reported in [10] whereas tortuosity values are taken from [18].

In porous media, Eq. (4) is modified to implement the dusty gas model (DGM) due to the impact of Knudsen diffusion in small pores. DGM can be formulated either using Fick's Law or Maxwell-Stefan approach to model the species balance [45]. Using the Maxwell-Stefan approach the DGM formulation can be written as [46]

$$\sum_{\substack{j=1 \\ j \neq i}}^{n} \frac{x_j\mathbf{N_i} - x_i\mathbf{N_j}}{D_{ij}^{eff}} + \frac{\mathbf{N_i}}{D_{i,Kn}^{eff}} = -\frac{1}{RT}\nabla p_i \tag{8}$$

Table 1
Source terms.

Mass and Species	$R_j = \pm \dfrac{i_{a/c}}{nF} M_j$	(18)
Momentum	$\mathbf{F} = \mathbf{u} \displaystyle\sum_j R_j$	(19)
Energy	$Q = (E_{\max} - V_{cell}) i_a$	(20)
Anode transfer current	$i_a = A_a \exp\left(-\dfrac{EA_a}{RT}\right) \left(\dfrac{x_{H_2} p}{x_{H_2}^{ref} p_{ref}}\right)^{\gamma_{H_2}} \left(\dfrac{x_{H_2O} p}{x_{H_2O}^{ref} p_{ref}}\right)^{\gamma_{H_2O}} \sinh\left(\dfrac{\alpha_a F}{RT}\eta_a\right)$	(21)
Cathode transfer current	$i_c = A_c \exp\left(-\dfrac{EA_c}{RT}\right) \left(\dfrac{x_{O_2} p}{x_{O_2}^{ref} p_{ref}}\right)^{\gamma_{O_2}} \sinh\left(\dfrac{\alpha_c F}{2RT}\eta_c\right)$	(22)

where $D_{i,Kn}^{eff}$ is the effective Knudsen diffusion coefficient which is calculated from Mason and Malinauskas [46] as:

$$D_{i,Kn} = \frac{4}{3}\frac{\varepsilon}{\tau}\sqrt{\frac{8RT}{\pi M_i}} r_p \qquad (9)$$

Knudsen diffusion coefficient is calculated for each species separately. In Eq. (9) r_p is the average pore size.

Eq. (8) can be cast into a matrix form [47]

$$[\mathbf{B}](N) = -\frac{1}{RT}(\nabla p) \qquad (10)$$

which is converted for species diffusion flux by inversion of matrix [**B**]

$$(N) = -\frac{1}{RT}[\mathbf{B}]^{-1}(\nabla p) \qquad (11)$$

N is then used in Eq. (4) which replaces the second term inside the brackets on the left hand side.

2.3. Energy conservation

The conservation of energy for the entire domain is governed by:

$$\frac{d(\rho C_p T)}{dt} + \nabla \cdot \left(-k\nabla T + \rho C_p T \mathbf{u} + \sum_j h_j \mathbf{N_{D,j}}\right) = Q \qquad (12)$$

where the second term and third term inside the divergence account for heat transfer due to bulk convection and diffusion. These terms disappear in solid regions. Specific heat for the fluid mixture is determined via the expression

$$c_{p,mix} = \sum_j w_j c_{p,j} \qquad (13)$$

Although there are recommended expressions to estimate mixture thermal conductivity and viscosity [43], the values for N_2 is used for other mixture properties since both the air and fuel streams are largely comprised of N_2. On the other hand Ioara et al. [27]

Table 2
Geometrical parameters ([10] unless stated otherwise).

Property	Value
Inner anode diameter	0.8 mm
Anode thickness	0.4 mm
Electrolyte thickness	30 μm
Cathode thickness	70 μm
Anode length	10 mm
Electrolyte length	10 mm
Cathode length	7 mm
Anode porosity (after reduction of NiO), ε_a	0.45
Cathode porosity, ε_c	0.55
Anode tortuosity, τ_a [18]	3.5
Cathode tortuosity, τ_c [18]	3.5

reported that neglecting variations of the gas stream properties along the gas channels has a significant impact on both steady state and transient results, therefore fluid properties for a single species are defined as functions of temperature using the thermodynamic property tables found in [48].

In the porous regions heat equation is formulated by volume averaging as described in [49]. Assuming thermal equilibrium between the gas phase and the solid phase, the volume averaging results in the same form of Eq. (12), with modifications to the transient and conduction term. In the porous domains effective ρC_p and thermal conductivity are introduced in the transient and conduction terms respectively such that $(\rho C_p)_{eff} = \varepsilon(\rho C_p)_f + (1-\varepsilon)(\rho C_p)_s$ and $k_{eff} = \varepsilon k_f + (1-\varepsilon)k_s$. Since the thermal capacity (ρC_p) of the solid phase is much larger than that of the fluid phase, contribution of the fluid is neglected in the transient term.

The radiation heat transfer between the outer boundaries of the cell (as well as the alumina tube) and the furnace walls are modeled as a boundary conditions:

$$\mathbf{n} \cdot (\mathbf{q}_1 - \mathbf{q}_2) = \alpha_{abs}\varepsilon_{sb}(T^4 - T_{wall}^4); \quad \mathbf{q_i} = -k_i\nabla T_i + \rho_i C_{p,i} T_i \mathbf{u_i} \qquad (14)$$

2.4. Charge conservation

Since the characteristic time scale for charge transfer are much smaller than those for heat and mass transfer [30], ionic and electronic charge conservation equations are solved in steady state.

$$-\nabla \cdot (\sigma_e \nabla \phi_e) = j \qquad (15)$$

$$-\nabla \cdot (\sigma_i \nabla \phi_i) = -j \qquad (16)$$

Source terms in these equations are the charge transfer rates calculated via Butler-Volmer equations and are listed in Table 1.

To account for the current leaks through the electrolyte, the following electronic current is given as a flux boundary condition to the electronic charge equation (Eq. (15)) at the anode electrolyte interface:

$$-\mathbf{n} \cdot (\sigma_i \nabla \phi_i) = j_{leak}; \quad j_{leak} = \frac{\phi_{eq} - \phi_{e,c}}{L}\sigma_{i,elc}\left(\frac{p_\theta}{p_{O_2,c}}\right)^{1/4}$$

$$\times \frac{\exp((F/RT)\phi_{e,c}) - 1}{1 - \exp(-(F/RT)(\phi_{eq} - \phi_{e,c}))} \qquad (17)$$

At the cathode electrolyte interface, same flux is given as a flux boundary condition to the electronic charge equation. Eq. (17) derived by Riess [50] is the analytical solution to the electronic charge transfer equation in the electrolyte.

3. Numerical method

Model equations are implemented in a commercial multiphysics software, COMSOL, which uses finite element method to discretize the partial differential equations (PDEs). For transient problems
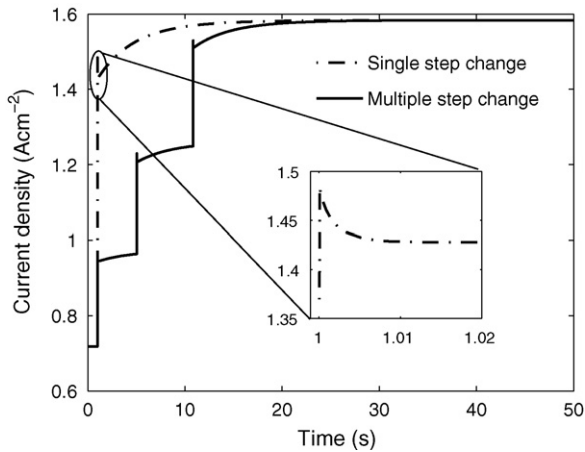
Fig. 2. Current density response of the SOFC to (i) single step change in voltage from 0.7 to 0.4 V at $t = 1$ s (dashed line), (ii) multiple step change in voltage from 0.7 to 0.6 V at $t = 1$ s then 0.6–0.5 V at $t = 6$ s and 0.5–0.4 V at $t = 11$ s (solid line). The insert shows the very initial time intervals of the current response for the single step case to show the overshoot phenomena.

COMSOL uses (vertical) method of lines in which it first discretizes the PDEs in the space domain [51]. After reducing the equation system to a set of non-linear ordinary differential equations (ODEs), COMSOL uses DASPK (differential-algebraic solver preconditioned Krylov) algorithm to solve for the new set of equations. DASPK algorithm developed by Brown et al. [52] is an implicit time-stepping scheme which implies that equation system of ODEs is solved in each time step. Non-linear set of equations is first solved with Newton iteration and then one of the linear solvers in COMSOL's library is employed in the rest of the solution.

Spatial discretization is carried out with 3799 triangular and 1940 quadrilateral mesh elements. Use of different element types in the same model allows us to adjust the mesh to cut down computational time while ensuring the accuracy. Time intervals are chosen as small as 10^{-4} in the vicinity of the step changes whereas time steps are chosen in the order of seconds near steady state. The solution takes from 5 min to 1 h depending on the time stepping chosen for specific analysis.

4. Results and discussion

Using the model described in the previous section, we have simulated multiple transient scenarios, first of which is the response to a change in operating voltage. For the following cases, the cell temperature is maintained at 550 °C and the cell runs on 3% relative humidity fuel composed of 5 ccm hydrogen and 20 ccm nitrogen while it uses ambient air (inside the furnace) on the cathode side.

4.1. Response to a change in cell voltage

Fig. 2 shows the dynamic responses of the current to a change in voltage from 0.7 to 0.4 V for two cases: (i) a single step change in voltage from 0.7 to 0.4 V at $t = 1$ s (dashed line); and (ii) a sequential step change in voltage first from 0.7 to 0.6 V at $t = 1$ s, then from 0.6 to 0.5 V at $t = 6$ s and then from 0.5 to 0.4 V at $t = 11$ s. In the sequential case, second and third steps are given at times when the current density reaches 98% of the steady-state values as a result of the previous inputs. For both cases dynamic response of the cell exhibits a sudden jump in current density at the instant when the step input is given due to the instantaneous electrochemical reaction taking place in the electrodes. It should be noted that the double-layer capacitance is not accounted in this model as the associated time scales are much smaller ($\sim 10\,\mu$s) than those of other
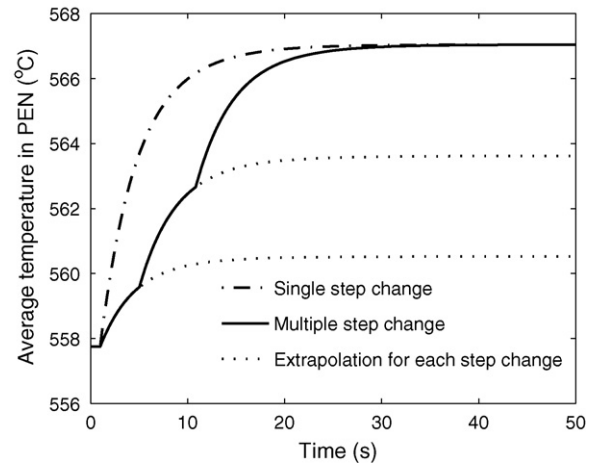

Fig. 3. Response of the average cell temperature to the voltage changes described in Fig. 2.

physical phenomena [33]. As a result of this momentary increase in current density, reactant concentration at the reaction sites drops instantaneously. Due to the larger mass transfer time scale from the channel to the electrodes, the reactants at the catalyst sites are not replaced instantly. The time scale for mass transfer is proportional to the diffusion time (e.g. δ^2/D), is calculated to be in the order of 3×10^{-3} s for anode 2×10^{-4} s for cathode. Consequently, concentration overpotential increases and hence the current density decreases for a period of time which results in an undershoot in the dynamic response of the cell. This can be seen in the insert of Fig. 2 which magnifies the very initial time intervals after the voltage change for single step case. It is observed that the undershoot lasts for 0.01 s which is similar to the time scale calculated for the mass transfer from the gas channel to the electrodes.

Following the undershoot, a transient regime of about 20 s is observed until the system reaches a steady state. This period is mainly governed by the temperature and is related to the heat transfer in the fuel cell. With a sudden increase in current density, the ohmic heat suddenly increases. As a result, temperature distribution changes inside the cell, however this process is considerably slower. Time scale for heat transfer is in the same order of magnitude with the thermal diffusion time, δ^2/α, which is calculated as 40 s. When the single step case is compared to multiple step case, it is seen that the current response of the latter is somewhat slower, although they reach the same steady state. To understand this difference, we compare the temperature responses. Increase in average cell temperature with respect to time is seen in Fig. 3 for both cases. In the single step case, average temperature in the positive/electrolyte/negative (PEN) rises from 558 to 567 °C in about 20 s. In the multiple step case, temperature first rises to 560 °C after the voltage changes from 0.7 to 0.6 V then it reaches to 563 °C after the second voltage change from 0.6 to 0.5 V and then it reaches 567 °C after the voltage drops to 0.4 V at $t = 11$ s. In this figure dotted lines represent the temperature responses for the cell when each step change is given as a standalone input to the system. If each standalone input is compared, it is seen that time scale for each case is identical. Indeed for a thermal system, represented with a first order differential equation (Eq. (12)), the time constant is independent of the step input but is inversely related to the effective thermal diffusivity ($k/\rho C_p$) of the system. The magnitude of the step only determines the final steady-state value. Hence time scale for the case when voltage drops from 0.7 to 0.6 V is same as the one for single input case when the voltage drops from 0.7 to 0.4 V which is about 20 s. So at $t = 11$ s when voltage is changed from 0.5 to 0.4 V, it is expected that the cell takes another 20 s to reach the
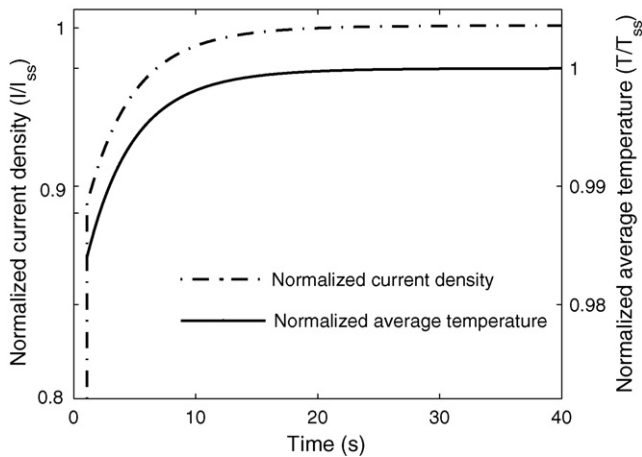
Fig. 4. Comparison of the overall time scale of the current density response (solid line) with that of temperature response (dashed line) to the single step change in cell voltage described in Fig. 2.

Fig. 5. Response of the average hydrogen mole fraction at the anode channel outlet to the voltage changes described in Fig. 2.

new steady state. As a result, the overall dynamics of the cell for the sequential input case is slower than that for single input case.

Another important observation in Fig. 3 is the rates of increase in temperature for both cases. For single input case the increase in temperature is sharper than that for the sequential input case, since for the latter the heat generation in the cell at each step change is much smaller than that for the single input case. Sudden changes in temperature have the risk of thermal shocks, which brittle SOFC materials may not survive. So from the thermal stress perspective, multi-step load change may be beneficial although it will delay the cell performance steady state.

As mentioned before the overall dynamics of the cell is governed by the thermal transients. Fig. 4 shows the correlation between the transients in current density and temperature, where the current density and temperature responses of the cell to the voltage change from 0.7 to 0.4 V at $t = 1$ s is plotted. For better comparison, current density (dashed line) and average cell temperature (solid line) are normalized with the final steady-state values. Because the dynamics of the current density until 1.01 s is associated with the instantaneous electrochemical reactions and the transients of the mass transfer, initial time intervals are not included in the plot. As seen, trends of both curves are identical reaching steady state at about 20 s. Note that current density increase is not linearly related to the temperature increase, since parameters determining the cell performance (e.g. ionic conductivity and exchange current density) are exponential functions of temperature.

Fig. 5 shows the average hydrogen mole fraction at the anode outlet as a function of time for single step and multiple step changes. At the instant of the step change in the voltage, instantaneous drop in hydrogen mole fraction is observed as result of sudden jump in the current density. After this initial drop, mole fraction decreases gradually until the overall system response becomes steady due to the increasing current density.

Current density profiles at the anode–electrolyte interface are shown in Fig. 6 for the step change in voltage from 0.7 to 0.55 V at $t = 1$ s. In Fig. 6a evolution of the ionic current density profiles during the overshoot is shown. Immediately after the change in voltage, current density increases up to 1.18 A cm^{-2}. After this sudden jump, the profiles evolve to lower values. Note that the cathode coating is shorter than the anode tube and reaction does not take place in parts of the anode where there is no corresponding cathode due to limited finite ionic conductivity. After the overshoot, current density increases gradually as seen in Fig. 6b. After $t = 7$ s, the change in the profile is not significant.
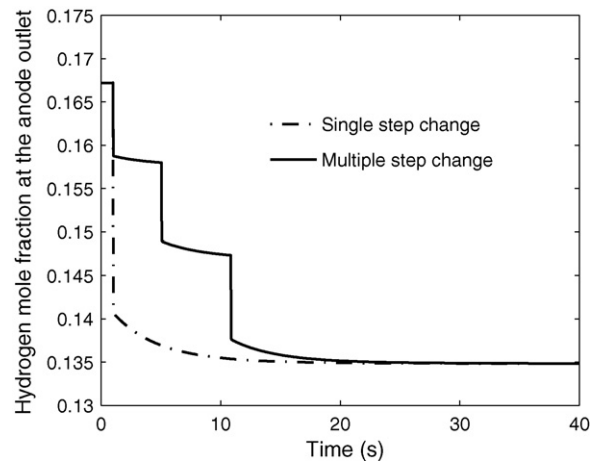
Corresponding temperature profiles at the same interface are seen in Fig. 7. The effect of sudden jump in the current density is not seen in the temperature response and the profile at $t = 1.2$ s is almost identical to the initial steady state. With the change in voltage from 0.7 to 0.55 V, maximum temperature in the cell increases from 561 to 573 °C. However, the increase is more in the first time steps as the maximum temperature reaches 565 °C 1.8 s after the voltage change
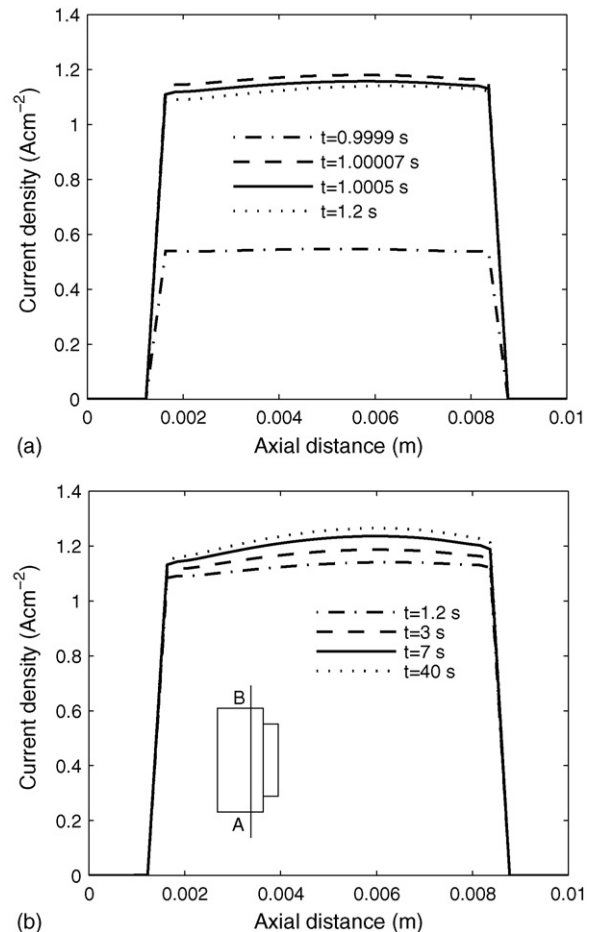

(a)

(b)

Fig. 6. Evolution of current density profiles along the anode–electrolyte interface for a change in the cell voltage from 0.7 to 0.55 V at $t = 1$ s a) during the overshoot, b) after the overshoot. Insert shows where the profiles are drawn in the cell.
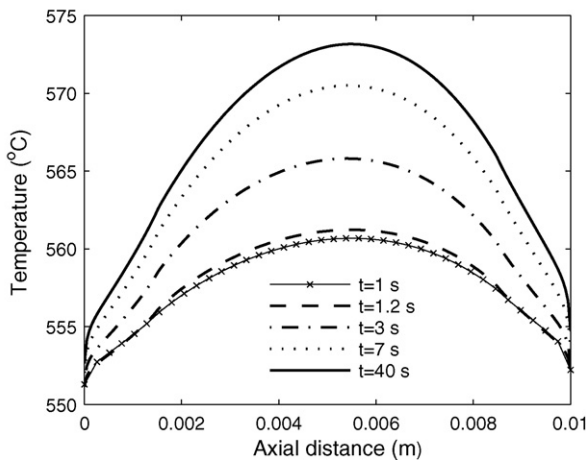
Fig. 7. Evolution of axial temperature profiles along the anode–electrolyte interface for the change in the cell voltage from 0.7 to 0.55 V at $t = 1$ s.

and then 570 °C 6 s after the voltage change. Maximum temperature in the cell is observed towards the outlet of the mid-point, since convective flow in the fuel channel distorts the symmetry of the temperature profile. As a result current density profiles are also distorted.

For the same input hydrogen mole fraction profiles are seen in Fig. 8 along the anode–electrolyte interface. Profiles 1–8 show the evolution of the hydrogen mole fraction at the interface until 1.0051 s. In this period profiles change significantly. This change is related to the dynamics of the mass transfer from the fuel channel to the electrode. Profiles 9, 10 and 11 correspond to 2, 5 and 40 s respectively. There is a little difference between these three profiles. This slow change is attributed to the slower dynamics of the heat transfer in the cell which results in a gradual increase in current generation hence a gradual decrease in hydrogen mole fraction. Recall that regions from 0 to 1.5 mm and 8.5 to 10 mm correspond to inactive anode regions.

4.2. Failure in the fuel supply system

We have also simulated a case involving a malfunction in the fuel supply system such as a pressure loss, due to a failure in the flow controllers or damage in the fuel line. In this failure scenario, we assume that fuel flow is shut-down in a very short period of time and we investigate possible outcomes of this situation.
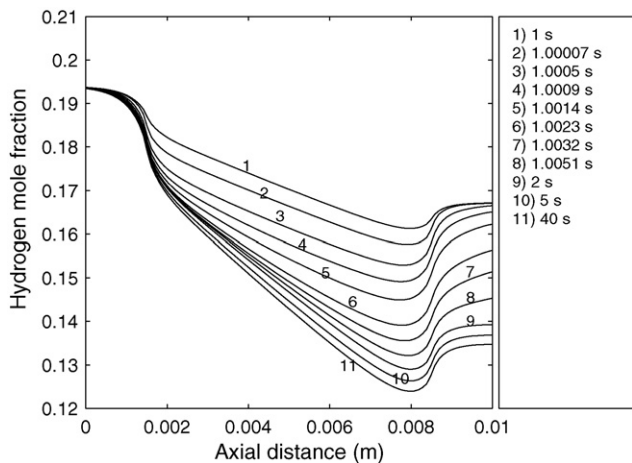

Fig. 8. Evolution of hydrogen mole fraction profiles along the anode–electrolyte interface for the change in the cell voltage from 0.7 to 0.55 V at $t = 1$ s.
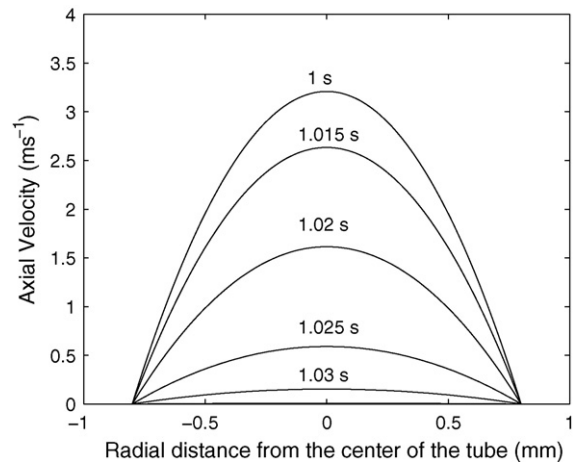

Fig. 9. Evolution of the velocity profile at the inlet of the fuel channel during the failure.

It is assumed that due to the failure in the fuel supply system at $t = 1$ s, the flow is completely stopped in 0.04 s. Fig. 9 shows the evolution of the velocity profiles at the fuel channel inlet. As inlet velocity decreases less hydrogen is carried to the anode. As a result the current density of the cell is presumed to be decreasing abruptly. Current density response of a micro-tubular SOFC operating at 0.7 V and 550 °C to this change in fuel supply at $t = 1$ s is seen in Fig. 10. Recall that ceria based electrolytes possess mixed conductivity, resulting in internal current leaks. Consequently, cell becomes short circuited and the operating current density is smaller than the ionic current density. In Fig. 10 both ionic current density (solid line) and operating current density (dashed line) are plotted. Even though there is still hydrogen in the fuel chamber to be used by the fuel cell till $t = 5$ s, the ionic current generated by the cell is not enough to compensate for the current leaks. Therefore in less than 1 s after the failure in the fuel supply system the fuel cell becomes incapable of generating *useful* (i.e. external) current.

Fig. 11 shows the evolution of the hydrogen mole fraction profiles at the anode electrolyte interface. Fig. 11a shows the profiles till the flow is completely stopped. Fig. 11b shows the profiles after the total fuel flow rate becomes zero. It should be noted that hydrogen and nitrogen flow rates decrease with the same rate thus the hydrogen mole fraction at the inlet stays constant until the flow stops completely. While there is flow at the inlet, hydrogen is car-
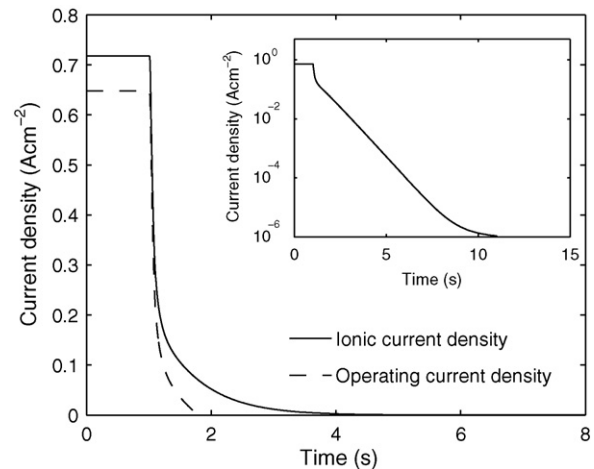

Fig. 10. Ionic (solid line) and electronic (dashed line) current density response of the SOFC to the cutoff of the fuel flow at $t = 1$ s. In the insert ionic current density response is plotted in logarithmic y-axis.
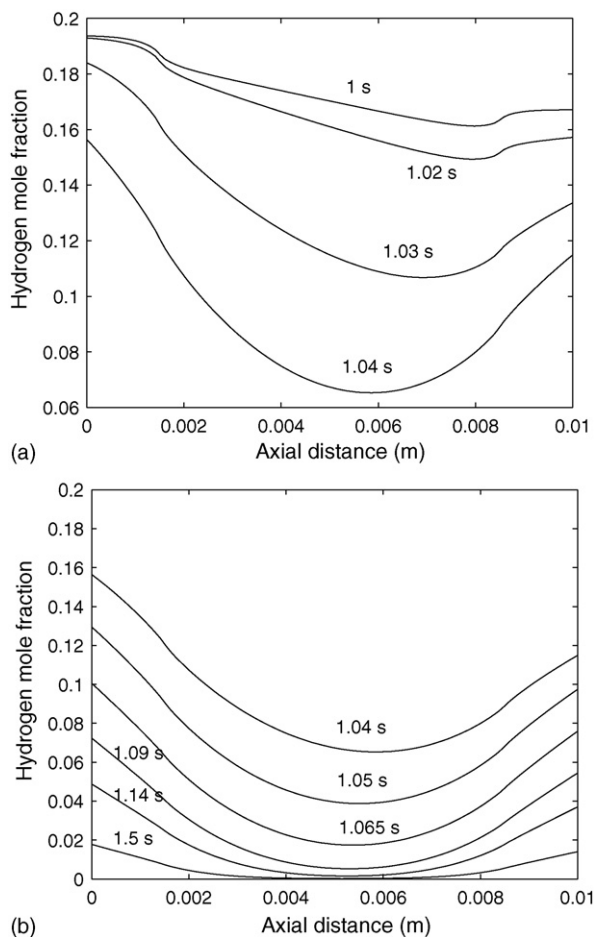
Fig. 11. Evolution of the hydrogen mole fraction profiles at the anode electrolyte interface a) during the flow rate is decreasing to zero b) after the fuel flow completely stops.

ried via both diffusion and convection. For $25\,cm^3\,min^{-1}$ of total fuel flow rate (at $t = 1\,s$) the maximum velocity in the center of the tube is $3.25\,m\,s^{-1}$. The effect of convective dominated process can be observed in hydrogen mole fraction profiles as they are flatter in the inactive anode regions and linear in the active anode regions. At $t = 1.02\,s$ mass transfer is still dominated by convection as the maximum inlet velocity is still as high as $1.6\,m\,s^{-1}$. The trend of the hydrogen mole fraction profile is very similar to the one before the failure. At $t = 1.03\,s$ flow rate is not zero yet, however the effect of convection decreases. This can be seen in the mole fraction profile as the curve becomes linear in the inactive anode regions and parabolic in the active anode region.

After the flow stops completely at $t = 1.04\,s$, remaining hydrogen in the fuel channel is carried to the anode purely by diffusion. Without the effects of convection, hydrogen mole fraction profiles evolve to be symmetric as seen in Fig. 11b and hydrogen diffuses to the anode from both inlet and outlet of the tube. In only 0.5 s hydrogen mole fraction decreases as low as 0.02 at the anode inlet but it takes 4 s for the cell to deplete nearly all the hydrogen in the surrounding gas channel completely.

5. Conclusion

A previously developed computational fluid dynamics (CFD) based SOFC model [36,37] is extended to analyze the dynamic behavior of a micro-tubular SOFC. Response of the cell to the changes in voltage is investigated. An overshoot is observed in the current density response as a result of the combined effect of fast electrochemical reaction and slower dynamics of the mass transfer. It is predicted that time-scales of a micro-tubular SOFC is in the order of 20 s governed by the dynamics of heat transfer. Response of the cell is also compared for two different voltage changes: (i) cell voltage is changed from 0.7 to 0.4 V as a single step input, (ii) cell voltage is changed from 0.7 to 0.4 V as a combination of three sequential step inputs. It is observed that the response of the multiple input case is slower. We also investigated the behavior of the cell in case of a failure in the fuel supply system. In the failure scenario we studied, the fuel flow is shut-down abruptly. Our results show that in case of a failure in the fuel supply system the cell reaction goes on for another 4 s till all the hydrogen in the channels is depleted completely. However, the cell stops generating output current 1 s after the failure. This is because after then the electrochemical reaction is not utilized by the external circuit due to internal current leaks. Similar behavior is also expected during normal shut-down of a ceria based SOFC.

References

[1] N.Q. Minh, T. Takahashi, Science and Technology of Ceramic Fuel Cells, Elsevier, Amsterdam, 1995.
[2] S. Livermore, J. Cotton, R. Ormerod, J. Power Sources 86 (2000) 411.
[3] V. Dorer, R. Weber, A. Weber, Energy Build. 37 (2005) 1132.
[4] A. Hawkes, P. Aguiar, C.A. Hernandez-Aramburo, M. Leach, N.P. Brandon, T.C. Green, C.S. Adjiman, J. Power Sources 156 (2006) 321.
[5] K. Alanne, A. Saari, I.V. Ugursal, J. Good, J. Power Sources 158 (2006) 403.
[6] N.M. Sammes, Y. Du, R. Bove, J. Power Sources 145 (2005) 428.
[7] K. Kendall, M. Palin, J. Power Sources 71 (1998) 268.
[8] W. Bujalski, C.M. Dikwal, K. Kendall, J. Power Sources 171 (2007) 96.
[9] T. Suzuki, T. Yamaguchi, Y. Fujishiro, M. Awano, J. Power Sources 160 (2006) 73.
[10] T. Suzuki, T. Yamaguchi, Y. Fujishiro, M. Awano, J. Electrochem. Soc. 153 (2006) A925.
[11] T. Suzuki, Y. Funahashi, T. Yamaguchi, Y. Fujishiro, M. Awano, Electrochem. Solid-State Lett. 10 (2007) A177.
[12] T. Suzuki, Y. Funahashi, T. Yamaguchi, Y. Fujishiro, M. Awano, J. Power Sources 171 (2007) 92.
[13] T. Suzuki, T. Yamaguchi, Y. Fujishiro, M. Awano, J. Power Sources 163 (2) (2007) 737.
[14] T. Yamaguchi, T. Suzuki, S. Shimizu, Y. Fujishiro, M. Awano, J. Membr. Sci. 300 (2007) 45.
[15] G. Buchinger, P. Hinterreiter, T. Raab, S. Griesser, R. Claassen, D.P. Claassen, W. Sitte, D. Meissner, J. Fuel Cell Sci. Technol. 3 (2006) 280.
[16] S. Hashimoto, H. Nishino, Y. Liu, K. Asano, M. Mori, Y. Funahashi, Y. Fujishiro, J. Electrochem. Soc. 155 (2008) B587.
[17] P. Costamagna, P. Costa, V. Antonucci, Electrochim. Acta 43 (1998) 375.
[18] H. Zhu, R.J. Kee, V.M. Janardhanan, O. Deutschmann, D.G. Goodwin, J. Electrochem. Soc. 152 (2005) A2427.
[19] S. Campanari, P. Iora, Fuel Cells 5 (2005) 34.
[20] V.M. Janardhanan, O. Deutschmann, J. Power Sources 162 (2006) 1192.
[21] P. Aguiar, D. Chadwick, L. Kershenbaum, Chem. Eng. Sci. 57 (2002) 1665.
[22] S. Ahmed, C. McPheeters, R. Kumar, J. Electrochem. Soc. 138 (1991) 2712.
[23] M. Iwata, T. Hikosaka, M. Morita, T. Iwanari, K. Ito, K. Onda, Y. Esaki, Y. Sakaki, S. Nagata, Solid State Ionics 132 (2000) 297.
[24] S. Nagata, A. Momma, T. Kato, Y. Kasuga, J. Power Sources 101 (2001) 60.
[25] Y. Qi, B. Huang, J. Luo, Chem. Eng. Sci. 61 (2006) 6057.
[26] E. Achenbach, J. Power Sources 49 (1994) 333.
[27] P. Iora, P. Aguiar, C.S. Adjiman, N.P. Brandon, Chem. Eng. Sci. 60 (2005) 2963.
[28] Y.M. Barzi, M. Ghassemi, M.H. Hamedi, Int. J. Hydrogen Energy 34 (2009) 2015.
[29] J. Jia, R. Jiang, S. Shen, A. Abudula, AIChE J. 54 (2008) 554.
[30] D. Bhattacharyya, R. Rengaswamy, C. Finnerty, Chem. Eng. Sci. (2009), doi:10.1016/j.ces.2008.12.040.
[31] T. Ota, M. Koyama, C. Wen, K. Yamada, H. Takahashi, J. Power Sources 118 (2003) 430.
[32] P. Nehter, J. Power Sources 157 (2006) 325.
[33] R.S. Gemmen, C.D. Johnson, J. Power Sources 144 (2005) 152.
[34] J. Padulles, G. Ault, J. McDonald, J. Power Sources 86 (2000) 495.
[35] A.M. Murshed, B. Huang, K. Nandakumar, J. Power Sources 163 (2007) 830.
[36] M.F. Serincan, U. Pasaogullari, N.M. Sammes, J. Electrochem. Soc. 155 (2008) B1117.
[37] M.F. Serincan, U. Pasaogullari, N.M. Sammes, J. Power Sources 192 (2009) 414–422.
[38] B.C.H. Steele, Solid State Ionics 134 (2000) 3.
[39] M. Godickemeier, L. Gauckler, J. Electrochem. Soc. 145 (1998) 414.
[40] C.F. Curtiss, R.B. Bird, Ind. Eng. Chem. Res. 38 (1999) 2515.
[41] E.N. Fuller, P.D. Schettler, J.C. Giddings, Ind. Eng. Chem. 58 (1966) 19–27.

[42] B.E. Poling, J.M. Prausnitz, J.P. O'Conell, The Properties of Gases and Liquids, fifth ed., McGraw-Hill, New York, 2001.
[43] B. Todd, J.B. Young, J. Power Sources 110 (2002) 186.
[44] L. Andreassi, G. Rubeo, S. Ubertini, P. Lunghi, R. Bove, Int. J. Hydrogen Energy 32 (2007) 4559.
[45] R. Suwanwarangkul, E. Croiset, M.W. Fowler, P.L. Douglas, E. Entchev, M.A. Douglas, J. Power Sources 122 (2003) 9.
[46] E.A. Mason, A.P. Malinauskas, Gas Transport in Porous Media: The Dusty-Gas Model, Elsevier, Amsterdam, 1983.
[47] R. Krishna, J.A. Wesselingh, Chem. Eng. Sci. 52 (1997) 861–911.
[48] Y. Cengel, M. Boles, Thermodynamics: An Engineering Approach, McGraw Hill, New York, 1994.
[49] A. Faghri, Y. Zhang, Transport Phenomena in Multiphase Systems, Academic Press – Elsevier Inc., Burlington, MA, 2006, p. 993.
[50] I. Riess, J. Electrochem. Soc. 128 (1981) 2077.
[51] COMSOL 3.4 Multiphysics Reference Guide, Burlington, MA, 2007.
[52] P.N. Brown, A.C. Hindmarsh, L.R. Petzold, J. Sci. Comput. 15 (1994) 1467.